Structural and magnetic properties of [001] $CoCr_2O_4$ thin films

Roger Guzman,[1,2] Jeroen Heuver,[3] Sylvia Matzen,[3] César Magén,[1,4,5,6,*] and Beatriz Noheda[3,†]

[1]*Laboratorio de Microscopías Avanzadas (LMA), Instituto de Nanociencia de Aragon (INA), Universidad de Zaragoza, 50018 Zaragoza, Spain*

[2]*Institut de Ciència de Materials de Barcelona, Consejo Superior de Investigaciones Científicas (ICMAB-CSIC), Campus de la Universitat Autònoma de Barcelona (UAB), 08193 Bellaterra, Spain*

[3]*Zernike Institute for Advanced Materials, University of Groningen, Nijenborgh 4, 9747 AG Groningen, The Netherlands*

[4]*Departamento de Física de la Materia Condensada, Universidad de Zaragoza, 50009 Zaragoza, Spain*

[5]*Fundación Agencia Aragonesa para la Investigación y el Desarrollo (ARAID), 50018 Zaragoza, Spain*

[6]*Instituto de Ciencia de Materiales de Aragón (ICMA), CSIC–Universidad de Zaragoza, 50009 Zaragoza, Spain*

(Received 12 April 2017; revised manuscript received 30 June 2017; published 7 September 2017)

The spinel $CoCr_2O_4$ (CCO) is one of the few bulk multiferroics with net magnetic moment. However, studies on the properties of CCO thin films are scarce. Here, we investigate the interplay between microstructure and magnetism of a series of CCO epitaxial thin films by means of x-ray diffraction, magnetometry, and aberration-corrected scanning transmission electron microscopy (STEM). Optimum pristine CCO films can be grown on a substrate with spinel structure ($MgAl_2O_4$), despite the large lattice mismatch of ∼3%. On the contrary, a substrate with lower lattice mismatch (∼1%) but with the rock salt structure (MgO) favors the degradation of the CCO crystal quality by forming antiphase boundaries (APBs), drastically weakening the magnetization, in agreement with reports for other spinel films. Nevertheless, our results also show that the type and number of APBs can be tuned by changing the growth temperature to favor the ferromagnetic alignment between antiphase domains, giving rise to a partial recovery of the magnetization.

DOI: 10.1103/PhysRevB.96.104105

I. INTRODUCTION

Materials in which magnetism and ferroelectricity coexist belong to the class of so-called multiferroic materials [1–6]. The possibility of having strong magnetoelectric coupling makes multiferroics interesting for new device applications, when the magnetic order can be controlled by an electric field [7,8]. However, multiferroics are rare materials and only present magnetoelectric coupling in special cases [3]. Spin-induced ferroelectricity can give rise to the desired coupling between the magnetic and electric orders [6]. In complex oxides, a particular spin arrangement, typically spin spiral, can break inversion symmetry and then induce an electric polarization. However, these types of materials often have antiferromagnetic order and do not show any net magnetic component, making them unsuitable for some of the most desirable applications.

One of the few transition metal oxides showing multiferroic properties with magnetoelectric coupling and a net magnetization is $CoCr_2O_4$ (CCO), [9–12] a cubic spinel that exhibits different magnetic phases, depending on the temperature: CCO orders ferrimagnetically below 93 K, while below 26 K, it displays an incommensurate conical spin spiral structure [13–19], with the rotating spin component lying within the (001) plane and the spontaneous magnetization along the [001] direction. This magnetic structure induces an electric polarization in the ⟨110⟩ direction by the inverse Dzyaloshinskii-Moriya interaction [20,21]. Yamasaki *et al.* showed that in the conical spiral magnetic state the polarization can be reversed repeatedly by a magnetic field [9].

For device applications, the integration of the material in the form of thin film is necessary. However, only a few studies have been focused on the epitaxial growth of CCO thin films [11,22–24]. Recently, experiments and theory revealed a strain dependence of the magnetocrystalline anisotropy in CCO thin films, where compressive strain induces a perpendicular magnetization, while tensile strain induces an in-plane magnetization [24]. This is relevant for the applications of magnetic thin films, as perpendicular magnetic anisotropy is more advantageous for high-density magnetic memories or spintronics applications [25]. The substrate used not only imposes the sign of the strain and the anisotropy but also the magnitude of the magnetization [24]: CCO films grown under compressive strain show larger magnetization than bulk single crystals, but the magnetization is lower for the films grown under tensile strain.

The growth of spinel films on rock salt structure materials, e.g., MgO, can result in the formation of antiphase boundaries (APBs), which may have a strong influence on material properties, such as lowering magnetization values with respect to bulk [26–29]. In fact, x-ray diffraction (XRD) measurements showed an excellent crystal quality for CCO films grown on $MgAl_2O_4$ (MAO) and a more defective lattice on those grown on MgO [24], even though the lattice mismatch is much higher in the case of MAO. Thus, the degradation of the crystal quality of CCO on MgO, and consequently of the magnetization, was attributed to the presence of APBs.

Here, we describe the influence of the deposition parameters on the morphology, epitaxy, and magnetism of high quality CCO thin films by means of XRD, magnetometry, and aberration-corrected scanning transmission electron microscopy (STEM). Combining geometrical phase analysis (GPA) with *Z*-contrast high angle annular dark field (HAADF) imaging in STEM, we examined the structure of defects in

*cmagend@unizar.es
†b.noheda@rug.nl

the films as a function of the deposition temperatures for a given substrate, MgO. Magnetometry experiments reveal that changing the growth temperature differently affects the magnetic properties of films, depending on the substrate used: while the magnetization is drastically reduced in CCO films deposited on MAO at high temperatures, in films deposited on MgO, there is a partial recovery of the magnetization values, reaching those observed in bulk. We evidence that this magnetization dependence with the growth temperature is mainly due to a change in the APBs characteristics (morphology, density, and crystallographic specifics) at high growth temperatures, favoring the ferromagnetic interaction between antiphase domains [30].

II. EXPERIMENTAL METHODS

The CCO thin films with thickness between 30 and 40 nm were grown by pulsed laser deposition on (001)-MgO and (001)-MAO cubic substrates, which have rock salt and spinel structure, respectively. The lattice mismatch values between CCO ($a = 8.33$ Å) and MgO ($a = 4.21$ Å) and MAO ($a = 8.08$ Å) are $+1.1$ and -3.1%, respectively. The structure of the thin films was determined by XRD, using an X'Pert laboratory diffractometer, and the magnetic properties were measured using a Quantum Design Magnetic Properties Measurement System (MPMS). For the temperature-dependence magnetization measurements, the samples were first cooled at 2 K/min in a field of 1 T down to 4 K. Then, at 4 K, the field was lowered to 0.01 T and stabilized for at least 1 h. Measurements were performed during warming up, with a ramp rate of 2 K/min. More details on the growth conditions and film structure have been described in Ref. [24].

For transmission electron microscopy studies, cross-sectional lamellae were fabricated by focused ion beam in an FEI Dual Beam Helios 650, while plane-view specimens were prepared by tripod mechanical polishing and low-voltage Ar+ ion milling. Aberration-corrected STEM analyses were carried out in a probe-corrected FEI Titan 60–300 microscope operated at 300 kV, fitted with a high-brightness field emission gun (X-FEG) and a corrected electron optical system (CEOS) probe aberration corrector. Atomic-resolution Z-contrast images were obtained by HAADF imaging in STEM, with a convergence angle of 25 mrad and a probe size below 1 Å. The detection semiangle range of the annular detector was calibrated at 48–200 mrad. The obtained raw images were filtered to reduce background noise.

The strain state of the CCO films was determined by GPA [31] of the HAADF images. Two consecutive 90° rotated images of the same area were taken to minimize scan distortions, and only the strain component along the fast scan direction was analyzed from each image. Changes in strain (measured in percentage) are determined relative to the substrate area, which is assumed a strain-free reference lattice. Defect-phase analysis was also carried out using the GPA tool by carefully selecting the diffraction spots in the Fourier transform.

The HAADF image simulations were performed with the STEM_CELL software [32,33], a simulation package based on the Kirkland routines [34]. This software is based on the multislice technique in the frozen-lattice approximation. The computed images were obtained using the same microscope experimental settings described above. The Kirkland routine for STEM simulation was used, setting the thermal diffuse scattering cycles to 20 and a sample thickness of about 4 nm. Source size broadening was taken into account using a Gaussian spread with 0.7 Å at full width at half maximum (FWHM).

III. RESULTS

A. Structural and magnetic characterization

The θ-2θ scans around the (004) CCO peak for films with different growth temperature are shown in Fig. 1 on MAO (a) and MgO (b), respectively. Both scans show that the increase in growth temperature results in decreasing peak intensity with weakening and the eventual disappearance of the Laue oscillations, i.e., the crystal quality decreases dramatically. The CCO peak position moves towards the substrate peak upon increasing temperatures, showing that higher growth temperature on both MgO (above 450 °C) and MAO, (above 400 °C) results in partial relaxation of the film (for lattice constants, see Tables I and II). However, films grown at 600 °C are not yet fully relaxed. The difference in the relaxation temperature for both substrates can be explained by the misfit between the CCO films and the substrates: the larger misfit strain of films on MAO results in relaxation at lower growth temperature (∼450 °C) than on MgO (between 500 and 600 °C). The out-of-plane lattice parameters extracted from θ-2θ scans, Figs. 1(a) and 1(b), and in-plane lattice constants determined from grazing incident XRD maps (not shown) are listed in Tables I and II. They are plotted as a function of the growth temperature in Fig. 1(c).

For those films, the apparent Poisson ratio, $\nu^* = (-\epsilon_{oop}/\epsilon_{ip})$, of the films was determined from the out-of-plane strain, $\epsilon_{oop} = (c - c_b)/c_b$, and in-plane strain, $\epsilon_{ip} = (a - a_b)/a_b$, with $c_b = a_b = 8.333$ Å, the CCO bulk lattice constant. The Poisson ratio (ν) can be calculated from ν^* by $\nu = \nu^*/(2 + \nu^*)$ [35]. A Poisson ratio of 0.5 is expected if no volume change of the unit cell occurs. On films on MAO, we observe Poisson ratio's in the range of 0.28–0.42, reflecting a small decrease in volume under compressive strain. These values are larger than the ones observed for $CoFe_2O_4$ (values of 0.2 and lower) [31,32]. For the films grown on MgO at 500 °C and below, the Poisson ratio is close to 0.5; thus, cell volume is preserved under tensile strain. The Poisson ratio's larger than 0.5 observed under tensile strain in samples on MgO at 600 °C are probably the result of defect formation (APBs) or Mg diffusion from the substrate, although at growth temperatures of 600 °C, no evidence of Mg was detected at the surface of the films by XPS, excluding major Mg diffusion from the substrate up to the surface. The CCO thin films exhibit highly anisotropic magnetic properties [24]. While the magnetization is found purely in-plane on MgO, the films deposited on MAO have an easy magnetization axis perpendicular to the film's plane. Temperature-dependent magnetization curves measured with the magnetic field applied both parallel and perpendicular to the film surface for CCO films on MAO and MgO are shown in Figs. 2(a) and 2(b), respectively. The ferrimagnetic transition temperature (T_c) of CCO thin films on MAO is dependent on the growth temperature. Films deposited at 600 °C have a

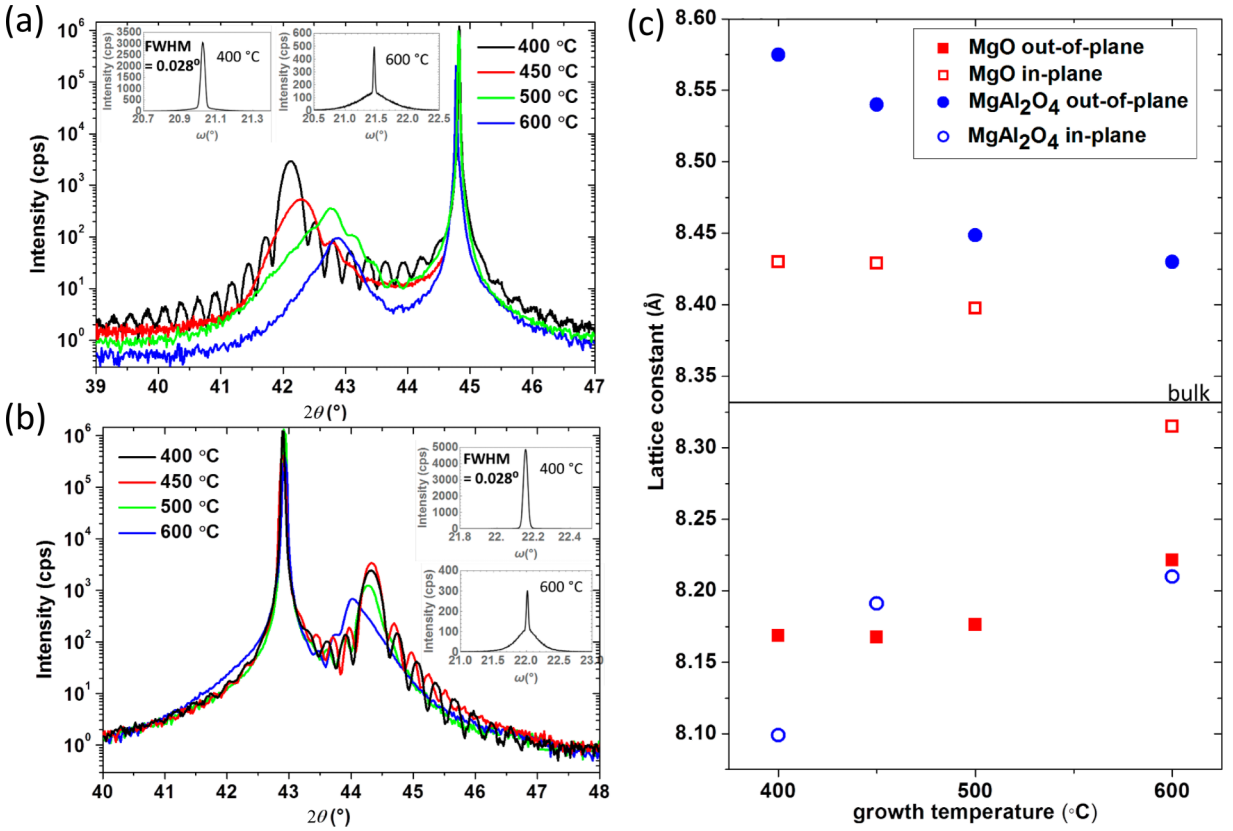

FIG. 1. The θ-2θ scans around (004) Bragg peak for CCO films (~40 nm) grown at different temperatures on MAO (a) and MgO (b), with in the insets the rocking curves for the films grown at 400 and 600 °C. (c) In-plane (open symbols) and out-of-plane (solid symbols) lattice constants of CCO films grown on MAO (circles) and MgO (squares) at different temperatures.

$T_c = 96$ K and low-temperature magnetization of 0.18 μ_B/f.u. at 0.01 T. The transition temperature is consistent with that reported in polycrystalline and single crystals [9,36]. However, the magnetization is larger than the values reported for single crystals and polycrystalline samples (0.08 μ_B/f.u. and 0.15 μ_B/f.u., respectively). On the other hand, samples grown at lower temperature have a lower T_c (down to 81 K), and increased magnetization (up to 0.34 μ_B/f.u.). The observed lower T_c in strained CCO films was already reported by Heuver *et al.* for both compressive and tensile strain [24]. Since films grown at low temperatures present a high crystal quality (no defects) and strain (see Fig. 1), this dependence of T_c with growth temperature must be related to the overall strain state rather than to the presence of APBs.

The magnetization of films on MgO is weaker than on MAO. The films deposited at 600 °C have a low-temperature magnetization of 0.06 μ_B/f.u. and $T_c = 93$ K, both close to bulk single crystals values. Samples grown at a temperature of 400 °C have an even weaker magnetization. For the samples grown at low temperatures, the temperature dependence of the magnetization is different than in the other samples: the magnetization starts to rise at 80 K, and it gradually increases with lowering the temperature, while the CCO films grown at 600 °C show a more abrupt magnetization change at T_c.

B. Strain state of the films

Epitaxial and fully strained CCO films can be grown on MgO and MAO at 400 and 450 °C, respectively, with excellent

TABLE I. Out-of-plane lattice constants (c), in-plane lattice constants (a), average lattice parameter ($\sqrt[3]{V}$), in-plane strain (ϵ_{ip}), out-of-plane strain (ϵ_{oop}), apparent Poisson ratio (ν^*), and the Poisson ratio (ν) of the CCO films on MAO shown in Fig. 1; V is the unit cell volume ($V = a^2c$).

T_{growth} (°C)	c (Å)	a (Å)	$\sqrt[3]{V}$ (Å)	ϵ_{ip}	ϵ_{oop}	ν^*	ν
400	8.575	8.099	8.255	−0.234	0.242	1.030	0.341
450	8.540	8.191	8.306	−0.142	0.207	1.460	0.422
600	8.430	8.210	8.283	−0.123	0.097	0.788	0.283

TABLE II. Out-of-plane lattice constants (c), in-plane lattice constants (a), average lattice parameter ($\sqrt[3]{V}$), in-plane strain (ϵ_{ip}), out-of-plane strain (ϵ_{oop}), apparent Poisson ratio (ν^*), and the Poisson ratio (ν) of the CCO films on MgO shown in Fig. 1; V is the unit cell volume ($V = a^2c$).

T_{growth} (°C)	c (Å)	a (Å)	$\sqrt[3]{V}$ (Å)	ϵ_{ip}	ϵ_{oop}	ν^*	ν
400	8.169	8.430	8.342	0.097	−0.164	1.69	0.459
450	8.167	8.429	8.341	0.096	−0.166	1.73	0.463
500	8.176	8.398	8.323	0.065	−0.157	2.43	0.548
600	8.221	8.315	8.284	−0.018	−0.112	−6.17	>0.5

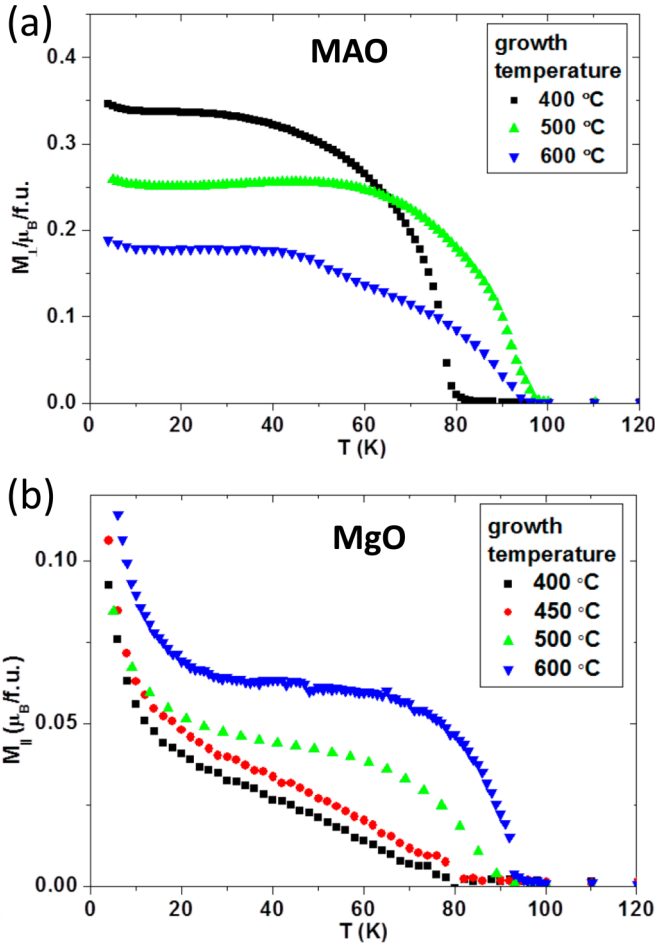

FIG. 2. Temperature dependence of the magnetization for CCO films grown at different temperatures. (a) Out-of-plane magnetization of CCO on MAO and (b) in-plane magnetization of CCO along the (001) axis on MgO.

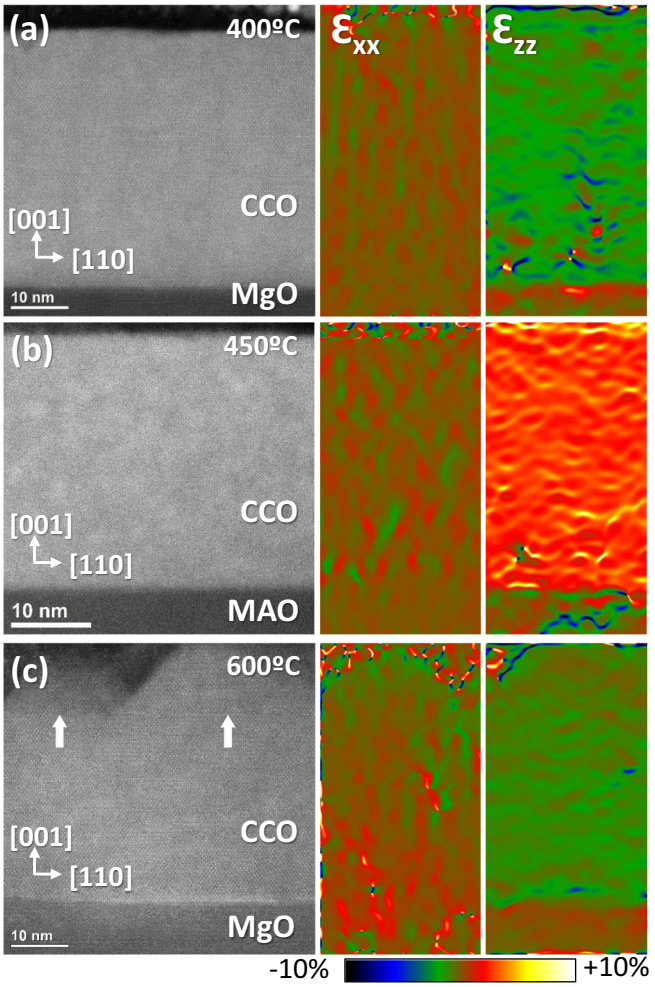

FIG. 3. Strain analysis of the CCO films grown on (a) MgO at 400 °C, (b) MAO at 450 °C, and (c) MgO at 600 °C. In-plane, ε_{xx}, (middle panels) and out-of-plane, ε_{yy}, (right panels) are a portion of the strain maps computed from HAADF images (left panels). Arrows in (c) point to the pyramids grown at the film surface.

quality and flat interfaces [24]. The high quality, strain state, and morphology of these films were corroborated by [110] cross-sectional HAADF-STEM images [Figs. 3(a) and 3(b)]. However, when growing at higher temperatures (600 °C), the morphology changes and results in roughening of both the substrate interface and the surface, as shown in Fig 3(c), where pyramids of 10 to 20 nm in height grow on top of the film surface showing {111} surface facets. The strain maps of the three films are shown in the central and right panels of Fig. 3, corresponding to the in-plane (ε_{xx}) and out-of-plane (ε_{zz}) deformation, respectively. In all cases, the ε_{xx} maps show no significant changes between the film and the substrate confirming that the films are fully strained. For ε_{zz} maps, as expected, the out-of-plane film lattice parameter changes according to the imposed strain (substrate): under tensile strain (on MgO) the c lattice parameter decreases, and under compressive strain (on MAO), c increases. Averaging over the whole film area, the out-of-plane parameters were determined. In the case of CCO/MgO at 400 and 600 °C the deformation values from GPA are $-2.3 \pm 0.3\%$ and $-2.0 \pm 0.3\%$, respectively, while in the case of CCO/MAO at 450 °C, the deformation is $+5.3 \pm 0.3\%$. This translates into a c lattice parameter of $c = 8.23$ Å, $c = 8.26$ Å, and $c = 8.57$ Å, respectively (bulk value is $c = 8.33$ Å). Note that these values are close to the ones measured by XRD: CCO/MgO (400 °C), $c = 8.17$ Å; CCO/MgO (600 °C), $c = 8.22$ Å; CCO/MAO, $c = 8.54$ Å (see Tables I and II).

C. Defect analysis: Effect of the growth temperature on the defect landscape in CCO/MgO films

As commented above, XRD around the [00l] Bragg peaks (specular reflections) shows that strained films grown on MAO exhibit high crystallinity both in the in-plane and out-of-plane directions. On the contrary, diffraction around off-specular reflections on MgO (not shown) display broadening of the peaks in the in-plane direction (absent in the films grown on MAO), evidencing a lack of crystal perfection that we address in APB formation [24].

The APBs are defect planes between two antiphase domains where the crystals on either side of the APB are related by a translation vector. These defects are well known in spinels [30,37–39] and can be imaged in a conventional TEM by

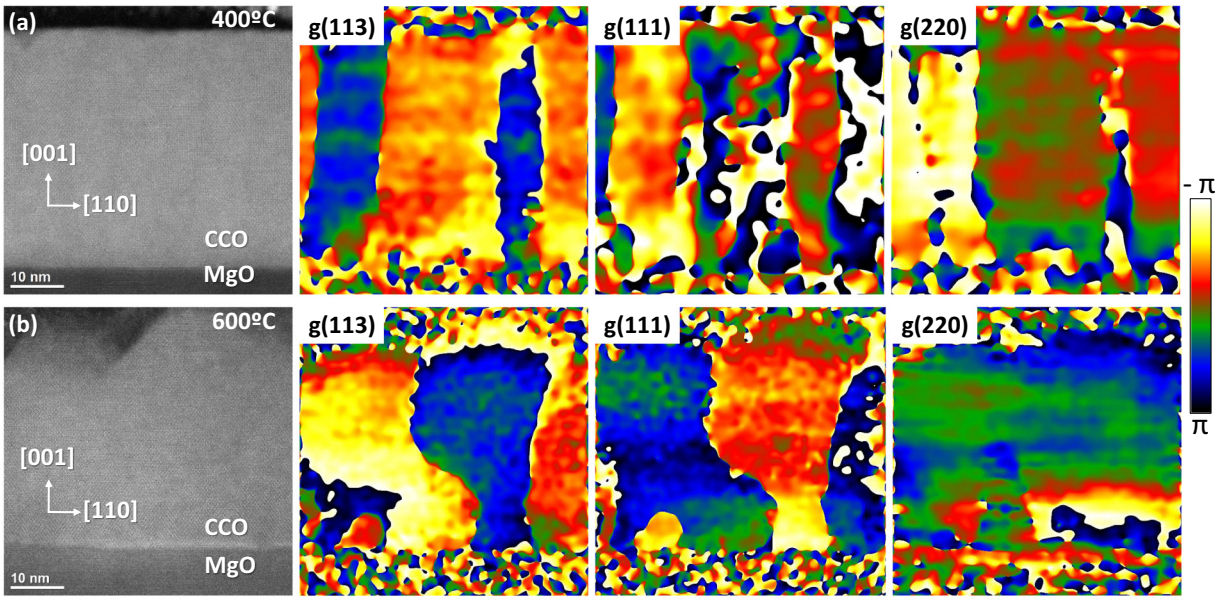

FIG. 4. The [110] cross-sectional HAADF images of the CCO samples grown on MgO at (a) 400 °C and (b) 600 °C, and their corresponding phase analysis for the (113), (111), and (220) **g** vectors.

dark-field imaging, where the crystal is tilted in such a way that only one diffracted beam related to this shift is highly excited, together with the direct beam, and this diffracted beam is selected to form an image of the specimen [40]. Then, an image of the intensity of this diffraction spot associated to a crystal defect is obtained. In this context, APBs are visible only when the phase shift $\alpha = 2\pi \mathbf{gR}$ is equal to $(2N + 1)\pi$, where **g** is the reciprocal vector corresponding to the diffracted beam, **R** is the shift vector of the APB, and N is an integer. Here, we used the GPA tool applied to atomic resolution HAADF images together with Bragg filtering to investigate the morphology of the defects as a function of the growth temperature for the films grown on MgO. When filtering the high-resolution images, the relative phase shift induced by the displacement of the fringes due to the antiphase disorder can be measured. Then, the specific shifts can be determined with a series of systematic phase images taken from different Bragg reflections (**g** vectors) and identifying whether the APB is visible or not.

Figure 4 shows the phase analysis of the (113), (111), and (220) **g** vectors from the HAADF images of the films grown on MgO at 400 °C and 600 °C, respectively. In the phase images, changes in the phase disorder (by a factor π) are due to the presence of APBs. For the reciprocal vectors **g**(113) and **g**(111), APBs with out-of-plane shift vectors are visible in both films. On the other hand, the phase analysis of the **g**(220) reveals APBs in the film grown at 400 °C but only a few in the bottom part of the 600 °C film [41]. Pure in-plane shift vectors also induce out-of-plane phase disorder when viewed along the [110] direction. Thus, according to the visibility criteria, only APBs with an out-of-plane shift component are visible, while **g**(113) and **g**(111) display both in-plane and out-of-plane shifts. In addition, another consequence is that those APBs common to all three reflections must contain in-plane shift vectors. As a result, we can conclude that both types of APBs (with pure in-plane shift and with out-of-plane component shift) are observed throughout the 400 °C film and at the bottom (closer to the substrate) of the 600 °C film. However, only pure in-plane shifts are found in the top part of the 600 °C film.

For 400 °C film, all observed APBs present boundary planes perpendicular to the surface. A detailed image of the APB structure of the films grown at 400 °C is shown in Fig. 5(a). According to the phase analysis of Fig. 4(a) in the **g**(111) and **g**(113) images, a phase change is expected for ¼[101], ¼[011], ¼[110], and ½[100] shift vectors. The crystal structure observed in Fig. 5(b) unveils that two different APB planes exist at the boundary, as evidenced by their characteristic patterns as a result of the overlapped spinel lattices. Three different crystal patterns can be distinguished and are labeled in Figs. 5(a) and 5(b). To help with the interpretation of these images, Fig. 5(c) shows three simulated HAADF images (top panels) computed from the crystal patterns (bottom panels) of a [110] spinel structure (I), an APB with ¼[110] or ½[100] shift vectors (II), and an APB with ¼[101] shift vector (III). These simulations confirm that the crystal pattern seen in region II corresponds to an APB with a purely in-plane component shift. On the other hand, the crystal pattern seen in region III is the expected pattern for an APB with out-of-plane component, as shown by the formation of planes of intense cation contrast forming an angle close to 55°, corresponding to {112} planes. The observed domains with APBs with pure in-plane components (region II) are much reduced in size (<5 nm) and are only seen in the presence of the larger domains (10 to 20 nm) with APBs with out-of-plane components. This explains the **g**(220) phase map in Fig. 4(a), where the phase shift is only observed in one of the two boundaries of the displayed domains.

Phase images (Fig. 4) reveal that the density of APBs is higher near the substrate interface for the film grown at 600 °C, where the domain size is reduced down to 5–10 nm. Contrary to the sample grown at 400 °C, APBs are not entirely perpendicular to the surface across the film thickness

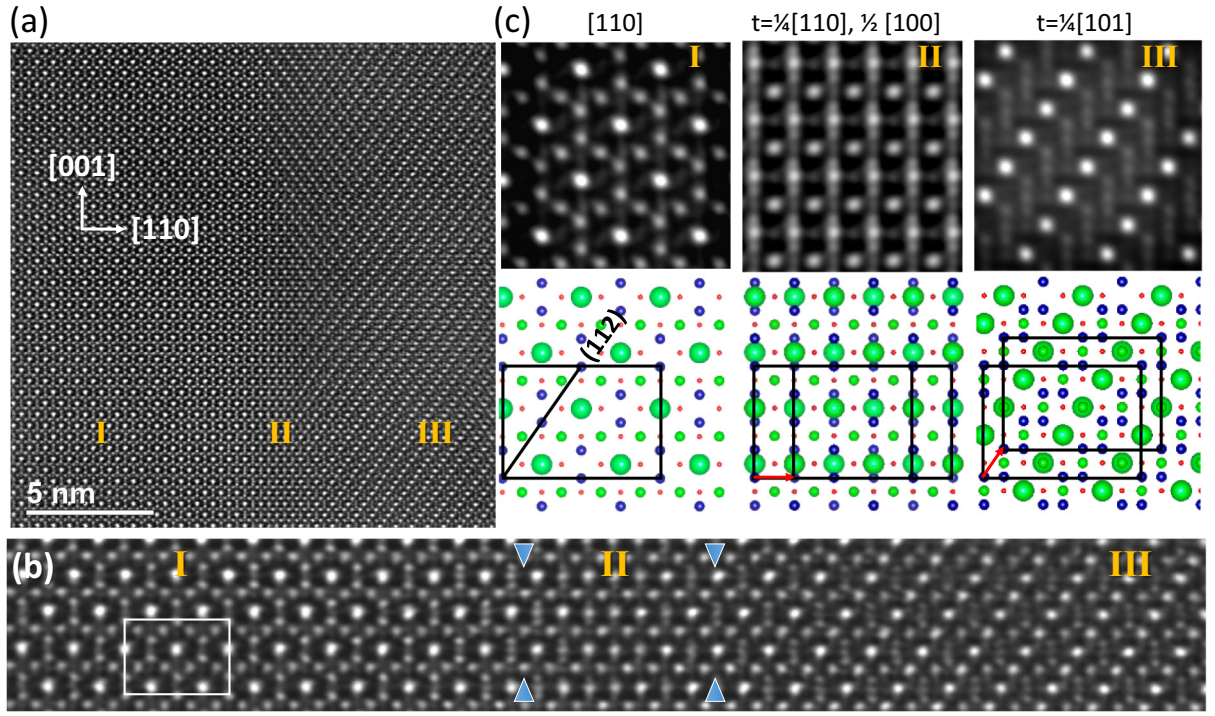

FIG. 5. (a) The HAADF image of the crystal structure at the APBs of the CCO films grown at 400 °C. (b) Close-up image from the bottom part showing the three different crystal patterns (numbered), as a result of the overlapped spinel lattices. The white square marks the spinel unit cell. The blue arrows mark the position of the APB planes. (c) The HAADF image simulations (top panels) for the three regions computed from the crystal structures (bottom panels). Region I corresponds to a perfect spinel lattice viewed along the [110] zone axis, while regions II and III correspond to APB with ¼[110] or ½[100] shift vectors and an APB with ¼[101] shift vector, respectively. The square marks the spinel unit cell, and the red arrow signals the translation vector. Co = blue; Cr = green; and O = red.

but curved. A close-up image of the film-substrate interface is shown in Fig. 6. Close to the substrate, the APBs are perpendicular to the interface, and above a certain critical thickness (∼10 nm), the boundaries curve running close to the {111} and {112} planes, i.e., at ∼35° and 55° to the film plane, respectively. Below the critical thickness, multiple contrast patterns occur due to the superposition of different domains with complementary shift components lying on both sides of the APBs. Here, the observed rhombic patterns are

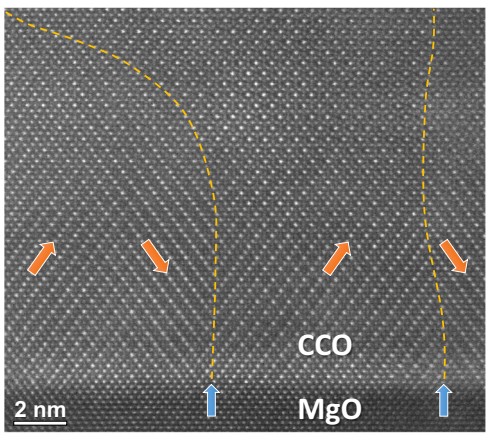

FIG. 6. The HAADF image of the CCO/MgO interface of a film deposited at 600 °C. The blue arrows point to the boundary planes, while the orange arrows mark the shift vectors direction.

the consequence of sets of adjacent domains with $\frac{1}{4}\langle 101\rangle$ and $\frac{1}{4}\langle -101\rangle$ shifts, where the planes of intense cation contrast along the ⟨111⟩ direction overlap (see Fig. 5). Close to the surface, the density of APBs is reduced, and the domain size increases.

Figure 7(a) shows the complex interaction of several APB planes occurring at the bulk of the film. The phase analysis from the same region is shown in Fig. 7(b), while Fig. 7(c) depicts close-up images of the different numbered regions. The phase images show the different APBs, and shift vectors can be determined. Regions Ia and Ib correspond to a perfect spinel structure viewed along the [110] zone axis. Between them, region II reveals a crystal pattern with ¼[110] or ½[100] shift vectors, Fig. 5(c), and then no phase shift is observed in the **g**(220) image. However, APBs with in-plane shift vectors ¼[110] or ½[100] are visible for both **g**(111) and **g**(-1-11). This corresponds to the case of the rightmost APB separating region Ib, which presents a curvature from the bottom part of the image until it becomes perpendicular up to the film surface. At the bottom, region III is divided in two parts, where region IIIa is invisible when **g**(111), and both regions IIIa and IIIb are invisible when **g**(-1-11). Then, regions IIIa and IIIb are associated to ¼[-101] and ¼[-10-1] shift vectors, respectively, with the latter being visible when **g**(111).

Contrary to the film deposited at 400 °C, APBs with pure in-plane shift vectors below the critical thickness are rarely seen at 600 °C, while they seem to dominate near the surface, as evidenced by the crystal pattern in region II in Fig. 7(c) and the phase analysis in Fig. 4. In addition, near the surface, APBs are

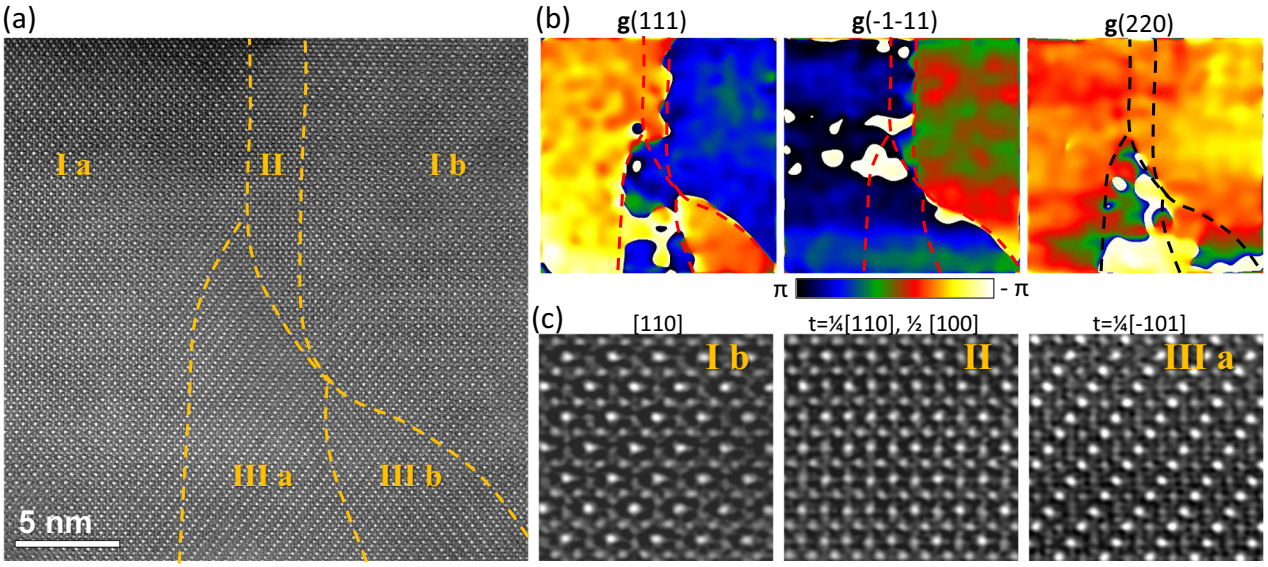

FIG. 7. (a) Detailed HAADF image of the interaction of several APBs near the surface of the CCO film grown on MgO at 600 °C. Different crystal regions are numbered, and the dashed lines delimitate the boundaries. (b) **g**(111), **g**(-1-11), and **g**(220) phase analysis of the same region. Dashed lines mark the position of the APBs. (c) Close-up images of the numbered regions in (a) where regions Ia and Ib correspond to a perfect spinel lattice viewed along the [110] zone axis, region II to APB with ¼[110] or ½[100] shift vectors and regions IIIa and IIIb correspond to APBs with ¼[-101] and ¼[-10-1] shift vectors, respectively.

no longer curved but perpendicular to the film. The curvature observed in the films grown at 600 °C can be attributed to the mobility of the APB planes. Eerenstein *et al.* showed that APBs are mobile, and they can be annealed out by diffusion resulting in larger domains when growing at higher temperature and longer annealing times [40]. They reported that after diffusion, boundaries become straighter and the number of junctions reduces. Nevertheless, in their work on the Fe_3O_4 spinel, they reported a growth temperature range 250–350 °C, much lower than the one we use to grow these CCO films. Then, we can conclude that the APBs in our films are more mobile above the critical thickness, resulting in curving and partial annealing of the APBs. This would explain the marked lower density of defects near the surface and the straightening of the boundary planes close to the surface.

To fully characterize the defects and determine the type of APB planes, the analysis was complemented with the observation of plane-view specimens. Two plane-view HAADF-STEM images of [001] CCO films grown on MgO at 400 and 600 °C are shown in Figs. 8(a) and 8(b), respectively. The direction of the APBs is indicated by the orange arrows in the HAADF image. Their corresponding **g**(220) phase analysis is shown in the central panels. The observed APB density is higher in the film grown at 600 °C, with domains widths below 15 nm, which suggests that the observed area in Fig. 8(b) corresponds to a section of the film near the substrate interface, from our previous cross-sectional analysis. The APBs should be viewed edge on from this projection, but the crystals at both sides of the plane overlap few unit cells (see right panels in Fig. 8). This might be explained due to the irregular shape of the quasistraight vertical boundary planes, as observed in the cross section. According to the visibility criteria, taking the **g**(2-20), only APBs with out-of-plane shift components are visible, i.e., ¼[011], ¼[0-11], ¼[101], and ¼[-101]. Indeed, as observed in both cases in the HAADF images at the APBs, the smoothed contrast at the empty octahedral sites reveal that these sites are apparently occupied by Co atoms, and this can only be addressed to APBs with out-of-plane shift vectors (see spinel structure on the HAADF image). This is consistent with the cross-sectional phase analysis of both samples, where APBs with ¼⟨101⟩ shift vectors dominate at low temperature growth and near the interface at high temperature growth. Unfortunately, APBs with pure in-plane shift vectors remain invisible along this crystal projection since those vectors preserve the crystal stoichiometry. Thus, the antiphase shift associated to the crystal patterns seen in the cross section (Figs. 5 and 7), either ½[100] or ¼[110], cannot be determined. However, since APBs with ½[100] shift vector are energetically unfavorable and hardly observed [30,39], it is most likely that these APBs have a ¼[110] shift vector.

IV. DISCUSSION

The density of defects is found to depend on the substrate and growth temperature. For the films grown on MAO at low temperature (450 °C), no presence of defects or a very low fraction is detected. However, a significant density of APBs is found in the films grown on MgO, and its amount depends on the growth temperature being larger in number at 600 °C than at 400 °C. Rocking curve measurements around the (004) reflection (see insets in Fig. 1) for both films grown on MAO and MgO corroborate the difference in the crystal quality for the two growth temperatures [24]: while the films grown at 400 °C show narrow rocking curves with FWHM of 0,028°, a clear broadening is observed in films grown at 600 °C.

One of the most relevant differences between the films grown on MgO is the crystallographic orientation of the APB planes. For the film grown at 400 °C, the APBs have preference for the {100} and {310} planes, while for the film grown at 600 °C, the APBs mainly run along the {110} planes. The

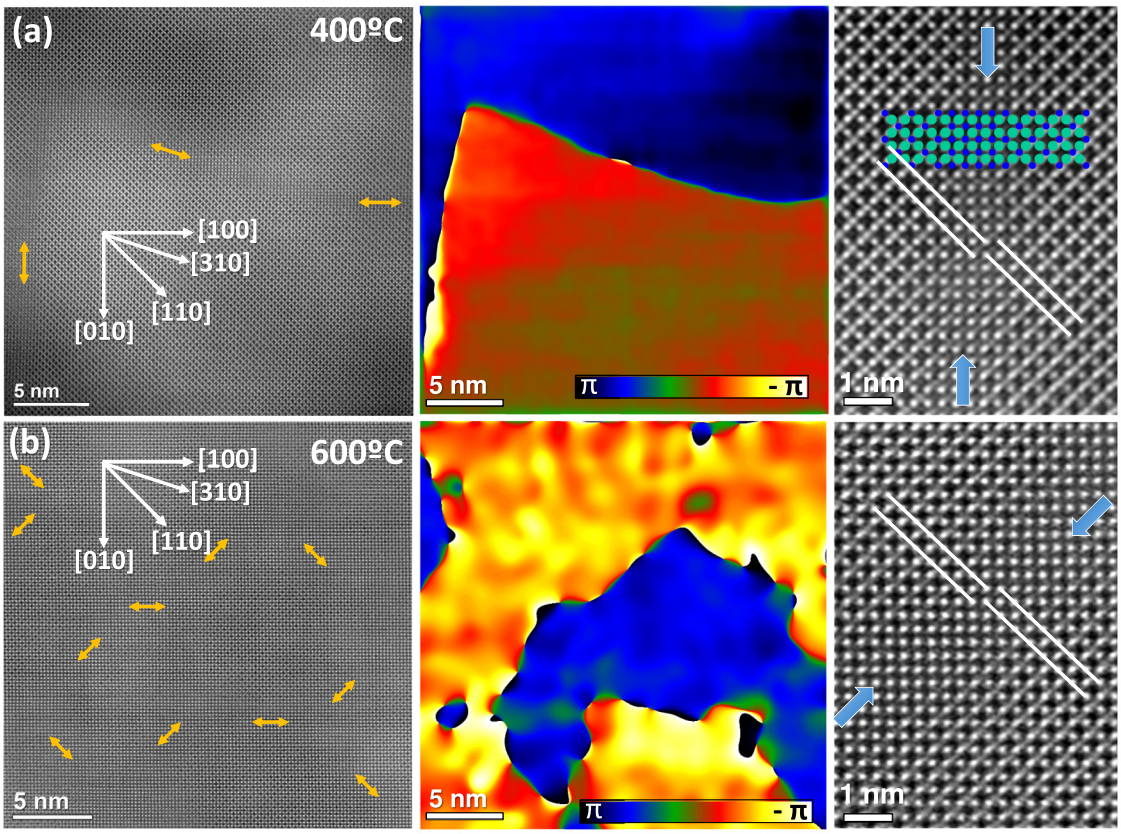

FIG. 8. Plane-view HAADF-STEM images (left panels) of the samples grown at (a) 400 °C and (b) 600 °C; (central panels), corresponding phase analysis taking the **g**(220) vector; (right panels), detailed HAADF images of the structure at the APBs, where blue lines indicate the crystallographic direction of the defects and white lines evidence the phase shift between domains. The CCO spinel atomic structure is shown: Co = blue; Cr = green.

relationship between antiphase shifts and boundary planes was extensively studied in several spinel structures and discussed in terms of APB energetics [30,39,40]. The APBs can minimize the energy either by minimizing the total APB surface area or the APB surface energy structure. The APBs with a shift vector perpendicular to the boundary plane keep the crystal stoichiometry and therefore are low in energy. Among APBs with a shift vector perpendicular to the boundary, those with $\frac{1}{4}\langle 100\rangle$ phase shift and $\{100\}$ boundary plane have a structure across the boundary with edge-sharing octahedra and tetrahedra, while a $\frac{1}{4}\langle 110\rangle$ shift vector in a $\{110\}$ boundary plane will result in only corner sharing and then less electrostatic repulsion and lower energy. This would explain the fact that shift vectors of the $\frac{1}{2}\langle 100\rangle$ type are hardly observed because these APBs anneal out much faster with temperature than the APBs with a $\frac{1}{4}\langle 110\rangle$ shift vector [30,39]. This is in agreement with other reports showing that the $\frac{1}{4}\langle 110\rangle$ APBs are more abundant [37–39,42,43]. For $\frac{1}{4}\langle 101\rangle$ out-of-plane shift vectors, the boundary plane is not perpendicular to the shift vector. This is the case for the APBs seen at the 400 °C film, Fig. 5, and at the bottom part of the 600 °C film, Fig. 6. In this case, the boundary planes are close to $\{100\}$ or $\{310\}$, Fig. 8. This increases the APB energy per surface unit, but it decreases the total APB surface area and can minimize the total energy [30,39]. In the films grown at 400 °C, the observed smaller cross-section of the crystal pattern with pure in-plane shifts (region II in Fig. 5) suggests that $\frac{1}{4}\langle 110\rangle$ shift vectors must be ascribed to the $\{100\}$ planes and $\frac{1}{4}\langle 101\rangle$ to the $\{130\}$. Overall, APBs with out-of-plane shift vectors seem to be more abundant than the pure in-plane, which, in fact, is in agreement with the cross-sectional and plane-view analysis showing a higher density of APBs with out-of-plane shifts in both films.

At high growth temperature (600 °C), cross-sectional STEM showed $\{111\}$-faceted pyramids formed on top of the film [Fig. 4(b)], and plane-view STEM showed APB planes along the $\langle 110\rangle$; see Fig. 8(b). The crystallographic orientation of the defects appears to be linked with the shape and size of the pyramids. The phase analysis in Fig. 4(b) evidences that APBs curve above the critical thickness and the edge of the pyramid grow at the intersection of the APB with the film surface, where the domain size delimits the size of the pyramid. Pyramids with $\{111\}$ facets distributed along the $\langle 110\rangle$ direction were also observed in films grown by rf magnetron sputtering between 600 and 800 °C, being variable in size depending on growth conditions and film thickness [44]. The roughening of the surface results in a larger surface area, but the $\{111\}$ spinel surface is found to be energetically favorable due to changes in the layer spacing at the surfaces, cation inversion, or surface reconstruction [45–47].

Furthermore, we see that both the growth temperature and the strain can tune the defect landscape, which influence the magnetic properties of the material. On both MgO and MAO films, the shape of the temperature-dependent magnetization

TABLE III. Summary of the APBs observed in the CCO films grown on MgO, their presence and density, and the magnetic exchange interactions (antiferromagnetic, AFM; ferromagnetic, FM) across the APBs, listed according to the growth temperature.

Shift vector	Boundary plane	Growth temperature	Presence in the film	APB density	Magnetic ex. interaction
½[010],¼[110]	(010)	400 °C	Bulk	High	AFM
¼[101]	(130)	400 °C	Bulk	High	AFM
¼[101]	(110)	600 °C	Bottom	High	AFM/FM
¼[110]	(110)	600 °C	Top	Low	AFM/FM

is very different from that of bulk CCO, even though the magnetization of the target is comparable to the temperature dependence reported for bulk in literature [9,36]. The lower magnetization of CCO on MgO in comparison with CCO on MAO can be attributed to the abundance of APBs in the films. The APBs are known to reduce the values of magnetization in ferrite spinel thin films with respect to those of the bulk [26–29]. As discussed previously, it is important to understand the crystallographic configuration of the APB because it might influence the magnetic coupling across the APB. When an APB is formed, new magnetic exchange interactions arise across the boundary due to the antiphase disorder or the removal of planes, which can compete, depending on their relative strength and sign [27,30,39]. The types of observed APBs, their presence and density, as well as the associated magnetic exchange interactions have been summarized in Table III for each sample.

We also see that the magnetization behavior of CCO on MgO, in comparison with CCO on MAO, can be explained by the type and density of APBs in the films for each growth temperature. Celotto *et al.* analyzed the multiple magnetic configurations occurring at different types of APBs in epitaxial Fe_3O_4 films on MgO (see Ref. [30]). They examined the structure, layer by layer, at the APB and described the new interactions across the boundaries generated due to the antiphase disorder. The different type of magnetic exchange interactions observed are listed and labeled in Table IV. On the one hand, they showed that when APBs with either ½[010] (or ¼[110]) shift and (010) boundary plane or ¼[101] shift and (130) boundary plane occur, the number of strong antiferromagnetic interactions at the APB (cation-anion-cation with $\theta = 180°$ and $\theta = 120°$) is increased [30]. These types of APBs result in the strengthening of the intrasublattice antiferromagnetic superexchange coupling across the APB, which reverse the spin couplings such that the structural boundary separates oppositely magnetized regions. This may explain the large saturation fields and weak magnetization at low magnetic fields in the films grown at 400 °C, which present APBs with ¼⟨110⟩ shifts and {100} planes and with ¼⟨101⟩ shifts and {130} planes. On the other hand, films grown at 600 °C present a higher density of APBs with ¼⟨101⟩ shifts near the substrate interface and ¼⟨110⟩ shifts near the film surface, both with {110} boundary planes. The APBs with ¼[110] shift and (110) boundary plane lead to a strong competition between the intra-sublayers with antiferromagnetic and ferromagnetic couplings, with both configurations being very similar in energy [30]. This also seems to be the case for the APB type with the out-of-plane shift vector ¼[101] and (110) boundary plane, which is not reported in the work of Celotto *et al.*, and we examined using the same procedure (Figs. 9 and 10). Figures 9(a)–9(d) show the succession of monolayers in the unit cell with the tetrahedral sites above and below the oxygen-octahedral plane, where examples of superexchange

TABLE IV. List of the different magnetic exchange interactions (antiferromagnetic, AFM; ferromagnetic, FM) occurring across APBs in epitaxial Fe_3O_4 films on MgO.[a]

Exchange interaction	Type and angle	Strength and sign	Presence
oct-ox-oct (IV)	Super, 180°	AFM, strong	At APB
tet-ox-tet (VI)	Super, ∼140°	AFM, strong	At APB
oct-ox-tet (VIII)	Super, ∼120°	AFM, strong	Bulk and APB
oct-ox-oct (V)	Super, 90°	FM, weak	Bulk and APB
tet-ox-tet (X)	Super, ∼70°	AFM, weak	At APB
oct-oct (III)	Direct	FM, weak	Bulk and APB
tet-tet (IX)	Direct	AFM, weak	At APB
oct-tet (VII)	Direct	FM, weak	At APB

[a]Reproduced from Celotto *et al.* [30].

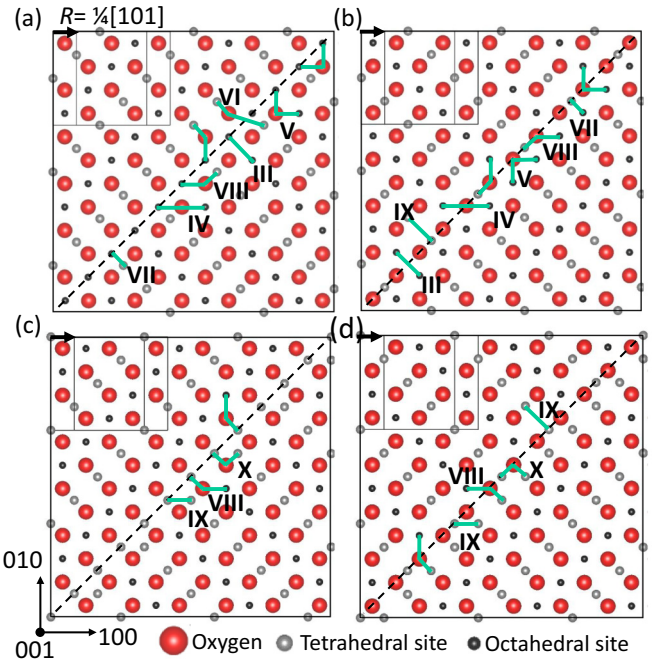

FIG. 9. Schematic drawing of a boundary with $R = ¼[101]$ shift (black arrow) and {110} boundary plane (dashed line). (a) Shows the first oxygen layer with the tetrahedral and octahedral sites just above and below the oxygen plane, and (b), (c), and (d) Show the successive layers. Examples of magnetic superexchange interactions across the boundary are indicated as green lines for each case.

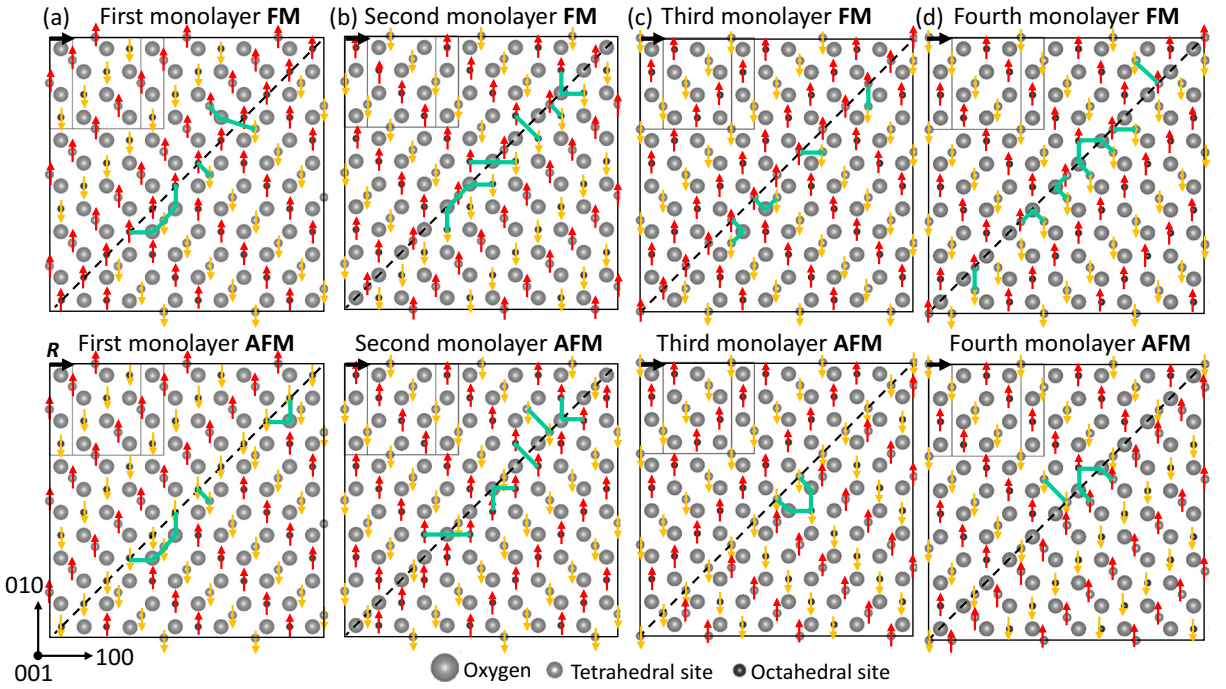

FIG. 10. Magnetic configurations for a boundary with $R = \frac{1}{4}[101]$ shift (black arrow) and $\{110\}$ boundary plane (dashed line). The magnetic moments are shown in colors for each monolayer, for both a ferromagnetic (FM) alignment (top panel) and an antiferromagnetic (AFM) alignment (bottom panel) between the two domains.

interactions are indicated by green lines. This is a more complex case where a great number of new superexchange interactions are generated at the boundary. In the case of the APB with the in-plane ¼[110] shift and (110) boundary plane, interactions are all competing across the boundary and not all of them can be minimized simultaneously, leading to frustration.

The magnetic configuration for each monolayer is examined in Figs. 10(a)–10(d), where the monolayers with an overall ferromagnetic (antiferromagnetic) alignment between domains are shown in the top (bottom) panels. The green lines display those interactions that cannot be minimized. In the first and second monolayers, Figs. 10(a) and 10(b), strong antiferromagnetic (IV, VI, and VIII) and weak ferromagnetic (III, VII, and X) interactions occur at the boundary. Some of the strong antiferromagnetic interactions (VIII, VI) can be minimized when the overall magnetic alignment is antiferromagnetic, but ferromagnetic interactions cannot be minimized with an overall ferromagnetic or antiferromagnetic alignment. Then, a ferromagnetic alignment between domains is favored in this case, as the total number of interactions minimized is higher. The opposite is true for the third and fourth monolayers, Figs. 10(c) and 10(d), where an overall antiferromagnetic alignment is favored. We then conclude that both configurations are probably very similar in energy and that the resulting alignment will depend on the interactions with other neighboring domains.

V. SUMMARY AND CONCLUSIONS

In this paper, we show that stoichiometric and fully strained CCO films with thicknesses up to 40 nm can be grown over a broad temperature range on top of MgO and MAO substrates. In both cases, low temperature growth results in flat, epitaxial, and fully strained thin films, while higher temperature growth gives rise to interface and surface roughening, as well as partial relaxation. In the particular case of CCO on MgO, temperature is a key parameter for the resulting APB characteristics, as reported for other spinel thin films. Our samples grown at 400 °C have $\{100\}$ and $\{130\}$ antiphase boundary planes (perpendicular to the film plane) with $\frac{1}{4}\langle 110\rangle$ and $\frac{1}{4}\langle 101\rangle$ shift vectors. At these APBs, strong antiferromagnetic couplings occur, having a remarkable influence on the magnetic properties of the films, resulting in a decrease of the magnetization. On the other hand, in samples grown at 600 °C, APBs curve above a critical thickness and straighten near the film surface. These films present a higher density of APBs on $\{110\}$ planes with $\langle 101\rangle$ shift vectors, which may favor the ferromagnetic alignment between antiphase domains and explain the partial recovery of the magnetization of these films.

To conclude, our TEM experiments demonstrate, first, that spinel CCO thin films can be grown defect free on spinel substrates. In addition, we show that for samples grown on rock salt substrates, the observed dependence of the magnetization with the growth temperature is due to the change in the type and number of APBs, in agreement to what was previously reported in the case of Fe_3O_4 Ref. [30]. These observations point to the generalization of the way in which different types of APBs modify the exchange interactions in magnetic spinels.

ACKNOWLEDGMENTS

Financial support is acknowledged from the European Union under the Seventh Framework Programme under a

contract for an Integrated Infrastructure Initiative Reference No. 312483-ESTEEM2, the Spanish Ministerio de Economía y Competitividad through Project No. MAT2014-51982-C2 and through the "Severo Ochoa" award Programme for Centres of Excellence in R&D (Project No. SEV-2015-0496), the Zernike Institute for Advanced Materials, The Netherlands, regional Gobierno de Aragón through Project No. E26, including Fondo Europeo de Desarrollo Regional (FEDER) funding.

R.G. and J.H. contributed equally to this work.

[1] N. A. Hill, J. Phys. Chem. B **104**, 6694 (2000).
[2] M. Fiebig, J. Phys. D. **38**, R123 (2005).
[3] W. Eerenstein, N. D. Mathur, and J. F. Scott, Nature (London) **442**, 759 (2006).
[4] Y. Tokura, J. Magn. Magn. Mater. **310**, 1145 (2007).
[5] T. Kimura, Annu. Rev. Mater. Res. **37**, 387 (2007).
[6] S.-W. Cheong and M. Mostovoy, Nat. Mater. **6**, 13 (2007).
[7] M. Gajek, M. Bibes, S. Fusil, K. Bouzehouane, J. Fontcuberta, A. Barthélémy, and A. Fert, Nat. Mater. **6**, 296 (2007).
[8] M. Bibes and A. Barthélémy, Nat. Mater. **7**, 425 (2008).
[9] Y. Yamasaki, S. Miyasaka, Y. Kaneko, J. P. He, T. Arima, and Y. Tokura, Phys. Rev. Lett. **96**, 207204 (2006).
[10] G. Lawes, B. Melot, K. Page, C. Ederer, M. A. Hayward, T. Proffen, and R. Seshadri, Phys. Rev. B **74**, 024413 (2006).
[11] X. Liu, M. Kareev, Y. Cao, J. Liu, S. Middey, D. Meyers, J. W. Freeland, and J. Chakhalian, Appl. Phys. Lett. **105**, 042401 (2014).
[12] Y. W. Windsor, C. Piamonteze, M. Ramakrishnan, A. Scaramucci, L. Rettig, and J. A. Huever, Phys. Rev. B **95**, 224413 (2017).
[13] N. Menyuk, K. Dwight, and A. Wold, J. Phys. **25**, 528 (1964).
[14] N. Menyuk, A. Wold, D. Rogers, and K. Dwight, J. Appl. Phys. **33**, 1144 (1962).
[15] S. Funahashi, Y. Morii, and H. R. Child, J. Appl. Phys. **61**, 4114 (1987).
[16] S. Funahashi, K. Siratori, and Y. Tomono, J. Phys. Soc. Jpn. **29**, 1179 (1970).
[17] K. Tomiyasu, J. Fukunaga, and H. Suzuki, Phys. Rev. B **70**, 214434 (2004).
[18] K. Dwight and N. Menyuk, J. Appl. Phys. **40**, 1156 (1969).
[19] V. Tsurkan, S. Zherlitsyn, S. Yasin, V. Felea, Y. Skourski, J. Deisenhofer, H.-A. Krug von Nidda, J. Wosnitza, and A. Loidl, Phys. Rev. Lett. **110**, 115502 (2013).
[20] M. Mostovoy, Phys. Rev. Lett. **96**, 067601 (2006).
[21] I. A. Sergienko and E. Dagotto, Phys. Rev. B **73**, 094434 (2006).
[22] Y. Suzuki, R. B. Van Dover, E. M. Gyorgy, J. M. Phillips, V. Korenivski, D. J. Werder, C. H. Chen, R. J. Cava, J. J. Krajewski, W. F. Peck, and K. B. Do, Appl. Phys. Lett. **68**, 714 (1996).
[23] U. Luders, F. Sanchez, J. Fontcuberta, U. Lüders, F. Sánchez, and J. Fontcuberta, Mater. Sci. Eng., B **109**, 200 (2004).
[24] J. A. Heuver, A. Scaramucci, Y. Blickenstorfer, S. Matzen, N. A. Spaldin, C. Ederer, and B. Noheda, Phys. Rev. B **92**, 214429 (2015).
[25] S. Mangin, D. Ravelosona, J. A. Katine, M. J. Carey, B. D. Terris, and E. E. Fullerton, Nat. Mater. **5**, 210 (2006).
[26] S. Venzke, R. B. Van Dover, J. M. Phillips, E. M. Gyory, T. Siegrist, C. H. Chen, D. Werder, R. M. Fleming, R. J. Felder, E. Coleman, and R. Opila, J. Mater. Res. **11**, 1187 (1996).
[27] D. T. Margulies, F. T. Parker, M. L. Rudee, F. E. Spada, J. N. Chapman, P. R. Aitchison, and A. E. Berkowitz, Phys. Rev. Lett. **79**, 5162 (1997).
[28] S. A. Chambers, R. F. C. Farrow, S. Maat, M. F. Toney, L. Folks, J. G. Catalano, T. P. Trainor, and G. E. Brown, J. Magn. Magn. Mater. **246**, 124 (2002).
[29] A. Lisfi, C. M. Williams, L. T. Nguyen, J. C. Lodder, A. Coleman, H. Corcoran, A. Johnson, P. Chang, A. Kumar, and W. Morgan, Phys. Rev. B **76**, 054405 (2007).
[30] S. Celotto, W. Eerenstein, and T. Hibma, Eur. Phys. J. B **36**, 271 (2003).
[31] M. J. Hÿtch, E. Snoeck, and R. Kilaas, Ultramicroscopy **74**, 131 (1998).
[32] V. Grillo and E. Rotunno, Ultramicroscopy **125**, 97 (2013).
[33] V. Grillo and F. Rossi, Ultramicroscopy **125**, 112 (2013).
[34] E. J. Kirkland, *Advanced Computing in Electron Microscopy*, (Plenum Press, New York, 1998).
[35] M. Foerster, M. Iliev, N. Dix, X. Martí, M. Barchuk, F. Sánchez, and J. Fontcuberta, Adv. Funct. Mater. **22**, 4344 (2012).
[36] N. Mufti, A. A. Nugroho, G. R. Blake, and T. T. M. Palstra, J. Phys.: Condens. Matter **22**, 075902 (2010).
[37] M.H. Lewis, Philos. Mag. **17**, 481 (1968).
[38] A.G. Fitzgerald and R. Engin, Thin Solid Films **20**, 317 (1974).
[39] O. Van Der Biest and G. Thomas, Phys. Status Solidi **24**, 65 (1974).
[40] W. Eerenstein, T. Palstra, T. Hibma, and S. Celotto, Phys. Rev. B **68**, 014428 (2003).
[41] There are seven types of shift vectors in spinels: one ½⟨100⟩ and six different ¼⟨110⟩ of which two, ¼ [110] and ¼ [1-10], are parallel to the film surface, and four shift vectors, ¼[101], ¼[-101], ¼[011], and ¼[0-11], have an out-of-plane component with a 45° angle to the surface.
[42] A. G. Fitzgerald and T. G. May, Thin Solid Films **35**, 201 (1976).
[43] H. Tabata, H. Okuda, and E. Ishii, Jpn. J. Appl. Phys. **12**, 7 (1973).
[44] U. Lüders, F. Sánchez, and J. Fontcuberta, Appl. Phys. A: Mater. Sci. Process. **81**, 103 (2005).
[45] W. Meyer, K. Biedermann, M. Gubo, L. Hammer, and K. Heinz, J. Phys.: Condens. Matter **20**, 265011 (2008).
[46] M. J. Davies, S. C. Parker, and G. W. Watson, J. Mater. Chem. **4**, 813 (1994).
[47] M. K. Rasmussen, K. Meinander, F. Besenbacher, and J. V. Lauritsen, Beilstein J. Nanotechnol. **3**, 192 (2012).